Localization of DivIVA by targeting to negatively curved membranes

Rok Lenarcic, Sven Halbedel, Loek Visser, Michael Shaw, Ling Juan Wu, Jeff Errington, Davide Marenduzzo, Leendert W. Hamoen

MATERIAL, METHODS & MODELLING

General methods

Molecular cloning, PCR reactions and *E. coli* transformations were carried out using standard techniques. *B. subtilis* chromosomal DNA for PCR reactions was purified as described by Venema *et al.* (Venema *et al.*, 1965). Clonings were checked by DNA restriction analyses and sequencing. SDS-PAGE, Coomassie staining, Western blotting, Bradford assays, and spectrophotometry, were performed following common protocols. Strains and plasmid used in this study are listed in Table S1, and primers are listed in Table S2.

Protein purifications

DivIVA-GFP was purified as a C-terminal hexahistidine tag. *divIVA-gfp* was amplified from pSG1612 (Edwards *et al.*, 2000) using primers div1 and div2, and cloned into expression vector pQE60 (Qiagen), resulting in pQEDG1. After induction and 2 h expression at 37 °C, *E. coli* cells were harvested followed by French Press and centrifugation. The supernatant was loaded onto a HiTrap Ni-affinity column (GE Healthcare), and washed with Wash buffer (20 mM Tris-HCl pH 8, 200 mM NaCl, 0.25 % Tween20), followed by Wash buffer without Tween20. The protein was eluted with an imidazole gradient (0-500 mM). Protein fractions were analysed with SDS-PAGE, and protein concentrations were determined with Bradford

assays or spectrophotometrically (A_{260}). Purified protein fractions were aliquoted, frozen in liquid N_2, and stored at -80 °C. GFP was purified by means of a C-terminal decahistidine tag (pQEG2), using essentially the same protocol as described for DivIVA-GFP purification.

DivIVA was purified using the IMPACT system (New England Biolabs). *divIVA* was amplified using primers div20 and div23, and cloned into pTYB1 (New England Biolabs), resulting in pTBD1. After induction and overnight expression at 16 °C cells were harvested. Cell extract was isolated using French Press followed by centrifugation, and the supernatant was loaded onto a chitin column using Loading buffer (20 mM Tris-HCl pH 8, 200 mM NaCl, 1 mM EDTA, 0.25 % Tween20). The column was washed with Loading buffer containing 1 M NaCl, followed by Cleavage buffer (20 mM Tris-HCl pH 8, 100 mM NaCl, 1 mM EDTA, 50 mM DTT). Intein cleavage occurred at 16 °C for 24 hrs. After elution of DivIVA the protein sample was further purified with a MonoQ column (GE Healthcare) using a salt gradient (20 mM Tris-HCl pH 8, 1 mM EDTA, 0-1 M NaCl). Protein fractions were analysed with SDS-PAGE, and protein concentrations were determined with Bradford assays or spectrophotometrically (A_{260}). Purified protein fractions were aliquoted, frozen in liquid N_2, and stored at -80 °C.

MBP-fusions were purified using the pMAL expression system (New England Biolabs). *divIVA* was cloned into pMAL2-C2 following a restriction free cloning method (van den Ent and Lowe, 2006), for which the following two primers were designed: LH65, and LH67, resulting in pMD1. After induction and 2 h expression at 37 °C, cells were harvested, followed by French Press and centrifugation. The supernatant was mixed with amylose resin (New England Biolabs) and loaded onto a gravity flow column (MoBiTec). The column was washed with Buffer A (20 mM Tris-HCl pH 8, 1M NaCl, 1 mM EDTA, 1 mM DTT, 0.25 % Tween20), Buffer B (20 mM Tris-HCl pH 8, 10 mM $MgCl_2$, 5 mM ATP, 150 mM NaCl, 1 mM β-mercaptoethanol, 0.25 % Tween20), and Buffer C (20 mM Tris-HCl pH 8, 100 mM

KCl, 1 mM EDTA), respectively. Deletion mutants of DivIVA-MBP were made by PCR and pMD1 as template (pDM2 = ΔC-DivIVA-MBP, primers LH71 andLH77, pDM3 = ΔN-DivIVA-MBP, primers LH21 and LH69). Purification of the deletion mutants was done according to the protocol described for full length DivIVA-MBP. Protein fractions were analysed with SDS-PAGE, and protein concentrations were determined with Bradford assays or spectrophotometrically (A_{260}). Purified protein fractions were aliquoted, frozen in liquid N_2, and stored at -80 °C.

RacA was purified as a MBP-RacA fusion. *racA* was amplified from *B. subtilis* chromosomal DNA using primers RL43 and RL44, and cloned into pMAL2-C2 using the restriction free cloning method. The resulting plasmid pRL10 was transformed into *E. coli* strain BL21. Expression of MBP-RacA was induced with IPTG when the culture reached an OD600 of ~0.5. After 2h cells were harvested followed by sonication and centrifugation. The supernatant was filtered, and loaded onto an amylase resin column (New England BioLabs). The column was washed with Buffer A (20 mM Tris-HCl pH 8, 200 mM NaCl, 1 mM EDTA, 0.5 mM DTT, 0.25 % Tween20), Buffer B (20 mM Tris-HCl pH8, 1 M NaCl, 1 mM EDTA, 0.5 mM DTT, 0.25 % Tween20), and Buffer C (20 mM Tris-HCL pH8, 100 mM NaCl and 0.5 mM DTT), followed by elution with Buffer C containing maltose. Protein fractions were analysed with SDS-PAGE, and protein concentrations were determined with Bradford assays or spectrophotometrically (A_{260}). Purified protein fractions were aliquoted, frozen in liquid N_2, and stored at -80 °C.

Detection of liposome clusters

The presence of DivIVA led to the aggregation of liposomes in the sucrose gradients. To examine this phenomenon in more detail, we mixed purified DivIVA with liposomes and looked at the mixture with a fluorescence light microscope. In these experiments liposomes

were labelled with the fluorescence membrane dye Nile Red. Liposomes were prepared by extrusion through a 0.4 μm pore filter as described before, and mixed (0.5 mg/ml final concentration) in 10 μl binding buffer (20 mM Tris-HCl pH 8, 200 mM KCl, 2 mM $MgCl_2$, 0.2 mM DTT, 2 mg/ml BSA). Purified DivIVA was centrifuged (5 min Eppendorf centrifuge, full speed) to remove protein aggregates, and 1 μl of the supernatant (0.04 mg/ml final concentration) was added to the liposome suspension. After a few minutes incubation 0.5 μl Nile Red solution (20 μg/ml) was added. The mixture was mounted onto a glass slide, and fluorescence images were obtained using a Zeiss Axiovert 200M (100x objective) microscope coupled to a CoolsnapHQ CDD camera, and Metamorph imaging software (Universal Imaging). An exposure time of 200 msec was used. Fig. S1 shows an example of such experiment, and the liposome clusters that were formed by DivIVA. In the control sample (no DivIVA) the fluorescence image is blurred due to the movement (Brownian motion) of floating liposomes.

Determination of the oligomeric state of DivIVA-MBP fusions

Removal of the N- and C-terminal domains of DivIVA might interfere with the formation of typical DivIVA oligomers. To test this, we determined the molecular weight of DivIVA-MBP complexes, and that of the truncated variants, using size exclusion chromatography. All three proteins were separated on a Superose^{TM} 6 10/300 GL gel filtration column (GE Healthcare). According to the elution profile, DivIVA-MBP is predominantly present as a complex with a molecular weight of 589 kDa (Fig. S2 A). Given a molecular mass of 70.3 kDa for DivIVA-MBP, these complexes are likely made up of 8 to 9 subunits, in accordance to previous reports (Muchova et al., 2002; Stahlberg et al., 2004). In case of DivIVA-ΔC-MBP (monomeric size 67.7 kDa) and DivIVA-ΔN-MBP (monomeric size 65.7 kDa) the prevailing forms are complexes that elude with retention times close to that of DivIVA-MBP. Therefore

the deletion of the N- and C-terminal amphiphatic helices does not seem to substantially influence oligomerisation.

Time lapse Microscopy

To test whether in *E. coli* DivIVA-GFP oscillates between the cell poles we followed several cell cycles using fluorescence light microscopy. Cells were grown in LB medium at 30 ºC to exponential phase when samples were taken and mounted onto microscope slides coated with a thin layer of 1.5 % agarose in LB medium. Fluorescence images were acquired every 10 min (exposure time 1 sec). Fig. S3 shows that the peripheral fluorescence signal increases during growth, and that the accumulation of DivIVA-GFP at the poles is related to the aging of the poles. Possibly, this is due to the inertia of cell poles compared to the continuously growing (rejuvenating) lateral wall (Lindner et al., 2008). We noticed no oscillation of the fluorescence signal.

Bacterial two-hybrid assay

Bacterial two hybrid analyses were carried out as described by Daniel *et al.* (Daniel et al., 2006) using a method based on Karimova *et al.* (Karimova et al., 1998). The test is based on the production of adenylate cyclase and consequently blue colonies on plates containing X-gal, if the two proteins interact. The coding sequence of *racA* was amplified by PCR and cloned into p25-N (low-copy plasmid for C-terminal adenylate cyclase T25 fragment fusion), pKT25 (low-copy plasmid for N-terminal adenylate cyclase T25 fragment fusion), pUT18 (high-copy plasmid for C-terminal adenylate cyclase T18 fragment fusion) and pUT18C (high-copy plasmid for N-terminal adenylate cyclase T18 fragment fusion) vectors using *XbaI* and *KpnI* restriction sites. The only positive interaction that we observed was between pUT18C-racA and p25-N-divIVA (Fig S4), where the adenylate cyclase fragment is fused to

the N-terminus of RacA, and the other part of adenylate cyclase is fused to the C-terminus of DivIVA.

Localisation of DivIVA in mutants defective in phospholipid biosynthesis

Three major species of phospholipids build up the cytoplasmic membrane of *B. subtilis* cells: phosphatidylethanolamine (PE), phosphatidylglycerol (PG) and cardiolipin (CL). Although initially thought to be distributed homogeneously throughout the whole membrane, recent work, using dyes specifically staining either PE or CL, has shown that both are enriched at the cell pole and septum (Kawai et al., 2004; Nishibori et al., 2005). Since DivIVA is a lipid binding protein, we considered the hypothesis that direct binding of DivIVA to a polarly enriched phospholipid species causes polar localisation. To test this hypothesis the localisation pattern of DivIVA-GFP in strains defective for PG, PE or CL was analyzed by fluorescence microscopy. In a conditional phosphatidylglycerophosphate synthase (required for PG) mutant (strain BSN7; *Pspac-pgsA*), localisation of DivIVA-GFP was indistinguishable from the control strain grown in the absence of IPTG (Fig. S5 B). Also, in the absence of phosphatidylserine decarboxylase (required for PE, strain BSN8) a normal localisation of DivIVA-GFP was observed (Fig. S5 C), suggesting that neither PG nor PE are essential for polar localisation of DivIVA. When DivIVA-GFP localisation was analyzed in a strain that contains the *clsA* gene, coding for cardiolipin synthase (Kawai et al., 2004) under control of *Pspac* (BSN9), no effect on the localization was observed in the absence of IPTG (Fig. S5 D). When the two *clsA* homologous genes *ywiE2* and *ywjE* were removed as well (BSN14), no alteration of the subcellular pattern of DivIVA-GFP was observed (Fig. S5 E), showing that the localisation of DivIVA does also not depend on CL.

DivIVA binding to liposomes of different diameter

Binding experiments were performed in binding buffer (20 mM Tris-HCl pH 8, 200 mM KCl, 2 mM $MgCl_2$, 0.2 mM DTT, 0.5 mg/ml BSA). Liposomes of different diameter were prepared by extrusion through 0.1 μm, 0.4 μm, or 5 μm pore filters. Liposomes (0.5 mg/ml) were mixed in binding buffer prior to the addition of different concentrations of purified DivIVA. After 20 min incubation at room temperature samples were centrifuged (Beckman TL-100 rotor, 80k rpm, 30 min, 30 ºC), and pellet fractions were analysed by SDS-PAGE and Coomassie staining. The intensity of DivIVA bands were measured by scanning the stained gels, and the results of such an experiment (repeated 3x) is presented in Fig. S6. Clearly, the affinity of DivIVA does not seem to depend on the diameter (positive curvature) of liposomes.

Measuring membrane curvature

To estimate the curvature of the membrane at *B. subtilis* division sites we used a transmission electron microscopic picture as shown in Fig. S7. The width of the cell is approximately 830 nm (Sharpe et al., 1998). We have drawn circles onto the EM picture using CorelDRAW software, and measured the radii. The average radius of the circles at the corners of the septum was 4.5 mm. At real scale this would correspond to a radius of 48 nm. The same was done with EM pictures of dividing *S. pombe* cells (based on (Osumi et al., 2006; Sipiczki and Bozsik, 2000)), which gave an average radius of approximately 60 nm (Fig. S8).

Monte-Carlo simulations of DivIVA accumulation in regions of high curvature

We performed Monte-Carlo simulations to study the thermodynamic and kinetic properties of a system of DivIVA oligomers (doggy bones), represented as diffusing spheres (25 nanometre diameter) in three dimensions, inside a bacterial cell. The rod-shaped cell was represented as a cylindrical membrane of dimensions 4 x 1 x 1 microns (length x diameter x diameter). The

dividing coccoid-shaped cell was modelled as a hemispherical surface with radius equal to 0.5 micron. The spheres feel a mutual interaction potential $V_{pp}(r)$ (*pp* stands for protein-protein interaction, r is the mutual distance between any two spheres, and the potential is measured in units of $k_B T$ in what follows), and are also attracted to the membrane via an interaction potential $V_{pm}(r')$ (*pm* stands for protein-membrane interaction, and r' is the distance between a sphere and the cell membrane(s), see below). The two potentials are modelled by two *square wells*. This means that when the distance, between two spheres (for V_{pp}) or between one sphere and the membrane (for V_{pm}), is smaller than an interaction range, which we take equal in both cases and call r_{int}, the two potentials are respectively constant and equal to their depths, which we measure in units of $k_B T$ (we recall that 1 $k_B T$ is approximately equal to 0.6 kcal/mol), and call E_{pp} and E_{pm} respectively. When the sphere-sphere distance or the membrane-sphere distance are larger than r_{int}, there is no interaction.

To determine the distance between the sphere and the cell membrane, we proceeded as follows. We focus on the rod-shaped cells for concreteness. In that case we computed the geometric distance from the centre of a given sphere to (i) the cylindrical surface (this is simply the difference between the cylinder radius and the two-dimensional distance between the axis of the cylinder and the point under investigation), and (ii) from either of the two planar membranes. It is therefore in principle possible that a single doggy bone sphere contacts two membranes at the same time (the cylindrical one and the top or bottom plane). This phenomenon would clearly increase localization, but this mechanism is also non-cooperative as it only relies on the competition between loss of entropy, due to going to the corners, and the enthalpic gain of having two rather than one contacts with a membrane (cooperative effects can still be important to join bound spheres into a ring, see below). It is not clear how realistic double membrane bonds may be *in vivo*, as there is no sharp corner in

a cell membrane (TEM images do show multiple contacts of doggy bones multimers with liposomes, but it is very difficult to draw conclusions about single doggy bones). EM pictures show that the radius of curvature at the corners of *B. subtilis* division septa is about 50 nm (Fig. S7). For this reason the cylindrical and planar membranes were joined by a smooth region with finite and variable radius of curvature R_c. [Note that we disregarded possible further contacts between spheres and the small joining membrane patch. This is an approximation which, if anything, will lead to a (small) underestimate of the localization at the high curvature corners.]

We also performed simulations with a variant of the model, in which there was no joining patch, but with the restriction that a sphere could only contact one membrane at a time. The results are similar to the one reported for the biologically relevant case of R_c of about 50 nm (indeed already for this curvature essentially no double membrane bonds occur). In the cocci simulations we have generalized the same procedure to compute the distance from the membranes.

The Monte-Carlo algorithm that we employed attempts to move one molecule at a time, by a small amount in the three-dimensional space. The new interaction energy felt by the particle which has undergone a trial move is then computed and compared with its old energy, and the move is subsequently accepted or rejected according to the standard Metropolis test (Allen and Tildesley, 1987; Binder and Heermann, 2002). This is done by comparing a random number, drawn with uniform probability between 0 and 1, with the minimum between 1 and $\exp(-\Delta E / k_B T)$, ΔE being the difference between the energy of the system before and after the move. This procedure is used to guide the system to the correct Boltzmann distribution in equilibrium. Provided that the moves are small enough and that the acceptance probability remains high, it has also been shown that this Monte-Carlo dynamics corresponds well to Brownian or molecular dynamics (Whitelam and Geissler, 2007),

although no attempt is made here to predict purely kinetic quantities. We took r_{int} equal to 15 nm (postulating smaller values of the interaction range do not qualitatively affect our results but would render the simulations slower as it would increase the rejection rate in the Metropolis test). To quantify localization, we defined a cut-off distance between either of the membranes, typically 200 nm, and stipulated that a given doggy bone sphere was localised in the high curvature region if it was within this cut-off distance (i) from both the cylindrical membrane and the planar surface. Simulations were run with 100, 200 and 400 particles with the results being qualitatively confirmed. Detailed effects of concentrations will be discussed elsewhere. The results in Fig. S9 are based on simulations with 200 particles, except for the last simulation in which 100 particles were used.

Simulation results

In Fig. S9 A we plot the fraction of localized spheres as a function of the radius of curvature R_c of the membrane patch separating the cylindrical and planar membranes. If $R_c = 0$, or very small, then the same sphere can make two contacts with different surfaces and as a result localization is very efficient. If a sphere can make further contacts (see below), these join up to form a ring. On the other hand, if R_c is very large then the spheres bound at either membranes do not feel each other and do not localize at the corners. For intermediate values of the radius of curvature, and most relevant to us, close to the *B. subtilis* curvature radius at the corners of septa (~ 50 nm), each sphere can contact just one membrane at a time, but the presence of intervening spheres attracted to the membrane-bound spheres can provide a bridge between spheres adsorbed on different membranes: as a result of this bridging interaction (see text) we still observe localization.

In Fig. S9 we present several cases, in which we make different assumptions on the total number of bonds that a sphere can make, either with other spheres or with the

membrane. For each case, we show the graph of the localized fraction of spheres as a function of radius of curvature, and the distribution of spheres, typically after 10 seconds of simulated time (see below for a note on the mapping between simulated and real time). In case I, we make no restrictions on the number of bonds that can be made. In the intermediate curvature regime large aggregates form and then slide to the high curvature regime where the cluster can provide the bridging interactions necessary for localization. Imposing no restrictions on the number of bonds may be a realistic assumption *in vivo* where depletion forces (due to macromolecular crowding) are present, as the depletion interactions are not limited in number (Zimmerman and Minton, 1993). This unrestricted case already shows the basic mechanism at work and may be general to a lot more proteins which stick to each other and to the cell membrane with in general different affinities. However, based on previous biochemical studies of DivIVA oligomers (doggy bones) (Stahlberg et al., 2004), and on the TEM results (see main text), we have considered additional cases in which the number of interactions was limited. In case II and III we limited the interactions which a sphere can have (before and after the Monte-Carlo update) to 4. In case II we postulate that only a single contact is used in membrane interaction, leaving 3 more available for further sphere contacts, whereas in case IV we assume that two bonds are used for membrane interaction, leaving two bonds available for further contacts with other spheres. In cases IV and V, we have assumed that the maximum number of contacts is either 6 or 8. Half of the binding sites were taken up by one membrane contacts in both cases. Localization is generally stronger if the number of interactions is larger (compare cases I and V with III and IV).

The asymmetric distribution observed (Fig. S9 B, C) is due to the fact that we started the simulations with an asymmetric distribution (see for an example of the initial situation Fig. 8 of the main text). This was done to keep the simulation time in reasonable limits, as a simulation of a single condition lasted on average 48 hrs of computational time with a serial

Intel 2.4 GHz processor, on a Linux Platform. The initial condition is quite important for cases in which localization only relies on cooperative molecular bridging. In particular for cases I, IV and V where the interaction energy is effectively larger due to a larger number of possible interactions, the dynamics are slow as it involves the formation and diffusion of large protein clusters, which are often attached to the surface (this leads to a further slowing down as diffusion is less efficient in two-dimensions). Even after our longest simulations (corresponding to about 30 seconds of real time, see below) a symmetrical distribution in the cylinder is not always achieved.

The modelling performed thus far considered DivIVA oligomers as spheres. This is useful in order to highlight the broadness and generic nature of the molecular bridging interaction that leads to localization at regions of high curvature. However, EM studies showed that DivIVA oligomers form elongated doggy bone-like structures, and it is therefore more realistic to describe them as rod-like particles. As molecular bridging purely relies on the combination of protein-protein and protein-wall activity, we expect it to occur regardless of the molecular shape, hence rod-like particles should produce qualitative similar results compared to spherical particles. To verify this, we have modelled a doggy bone as a rod, made up by 4 rigidly connected spheres (Fig. S10), each with a diameter of 6.25 nm, so that the dimensions of a rod were 25 nm x 6.25 nm x 6.25 nm. We generalized our Monte-Carlo dynamics to consider rotational as well as translational diffusion of the rods. Motivated by the EM images, we assume that only the top and bottom sphere (of a rod) will form the interactions. The magnitude of the interactions and the restrictions on contacts were chosen as for the spheres in case V (4 contacts for top and 4 contacts for bottom sphere, thus maximum 8 contacts per rod). Since every rod required the simulation of 4 spheres we limited the number of rods (particles) in the simulations to 100. The results obtained are shown in the last panel (case VI) of Fig. S9. It can be seen that the rods localize to the curved membrane as

well, in agreement with our assumption. Interestingly, it appears that with rods localisation persists up to larger radii of curvature.

Estimating real time from Monte-Carlo simulations

As mentioned previously, the Monte-Carlo algorithm employed attempts to move one molecule at a time, by a small amount, which we call here *dl*. It has been shown that this Monte-Carlo dynamics corresponds well to Brownian or molecular dynamics (Whitelam and Geissler, 2007), but how can one in practice convert the simulation units into a physical time scale? To estimate how long a Monte-Carlo step is in real time we proceeded as follows. We estimated the diffusion constant, D, of a sphere of size σ=25 nm that is undergoing Brownian motion inside the cytosol, which we can approximate by an aqueous solvent with viscosity equal to 5 centi-Poise (Luby-Phelps, 2000). In formulas, we have (by using Einstein-Stokes' formula which relates diffusion constant, viscosity and particle size)

$$D = \frac{k_B T}{3\pi\eta\sigma} \qquad (1)$$

which leads to a value of about 3.5 $\mu m^2/s$. Now, the timescale needed to diffuse a length comparable to the sphere's own size is given by:

$$\tau = \frac{\sigma^2}{D} \qquad (2)$$

which is about 0.18 ms. In simulation units (Monte-Carlo steps, or sweeps), $\tau = 6a_f/(dl)^2$, where a_f is the acceptance ratio (provided it is approximately constant in the simulations, both spatially and temporally). By equating τ in simulation and physical units, one may estimate that the duration of a single Monte-Carlo step is approximately 1-1.2 micro-seconds.

REFERENCES

Allen, M.P. and Tildesley, D.J. (1987) Computer simulations of liquids.

Binder, K. and Heermann, D.W. (2002) *Monte Carlo Simulation in Statistical Physics: An Introduction*.

Bramkamp, M., Emmins, R., Weston, L., Donovan, C., Daniel, R.A. and Errington, J. (2008) A novel component of the division-site selection system of *Bacillus subtilis* and a new mode of action for the division inhibitor MinCD. *Mol Microbiol*, **70**.

Daniel, R.A., Noirot-Gros, M.F., Noirot, P. and Errington, J. (2006) Multiple interactions between the transmembrane division proteins of Bacillus subtilis and the role of FtsL instability in divisome assembly. *J Bacteriol*, **188**, 7396-7404.

Edwards, D.H. and Errington, J. (1997) The *Bacillus subtilis* DivIVA protein targets to the division septum and controls the site specificity of cell division. *Mol. Microbiol.*, **24**, 905-915.

Edwards, D.H., Thomaides, H.B. and Errington, J. (2000) Promiscuous targeting of *Bacillus subtilis* cell division protein DivIVA to division sites in *Escherichia coli* and fission yeast. *EMBO J.*, **19**, 2719-2727.

Hamoen, L.W. and Errington, J. (2003) Polar targeting of DivIVA in *Bacillus subtilis* is not directly dependent on FtsZ or PBP 2B. *J Bacteriol*, **185**, 693-697.

Karimova, G., Pidoux, J., Ullmann, A. and Ladant, D. (1998) A bacterial two-hybrid system based on a reconstituted signal transduction pathway. *Proc Natl Acad Sci U S A*, **95**, 5752-5756.

Kawai, F., Shoda, M., Harashima, R., Sadaie, Y., Hara, H. and Matsumoto, K. (2004) Cardiolipin domains in *Bacillus subtilis* marburg membranes. *J Bacteriol*, **186**, 1475-1483.

Kobayashi, K. et al. (2003) Essential *Bacillus subtilis* genes. *Proc Natl Acad Sci U S A*, **100**, 4678-4683.

Korsak, D., Liebscher, S. and Vollmer, W. (2005) Susceptibility to antibiotics and beta-lactamase induction in murein hydrolase mutants of *Escherichia coli*. *Antimicrob Agents Chemother*, **49**, 1404-1409.

Lewis, P.J. and Marston, A.L. (1999) GFP vectors for controlled expression and dual labelling of protein fusions in *Bacillus subtilis*. *Gene*, **227**, 101-110.

Lindner, A.B., Madden, R., Demarez, A., Stewart, E.J. and Taddei, F. (2008) Asymmetric segregation of protein aggregates is associated with cellular aging and rejuvenation. *Proc Natl Acad Sci U S A*, **105**, 3076-3081.

Luby-Phelps, K. (2000) Cytoarchitecture and physical properties of cytoplasm: volume, viscosity, diffusion, intracellular surface area. *Int Rev Cytol*, **192**, 189-221.

Matsumoto, K., Okada, M., Horikoshi, Y., Matsuzaki, H., Kishi, T., Itaya, M. and Shibuya, I. (1998) Cloning, sequencing, and disruption of the *Bacillus subtilis psd* gene coding for phosphatidylserine decarboxylase. *J Bacteriol*, **180**, 100-106.

Muchova, K., Kutejova, E., Scott, D.J., Brannigan, J.A., Lewis, R.J., Wilkinson, A.J. and Barak, I. (2002) Oligomerization of the *Bacillus subtilis* division protein DivIVA. *Microbiology*, **148**, 807-813.

Nishibori, A., Kusaka, J., Hara, H., Umeda, M. and Matsumoto, K. (2005) Phosphatidylethanolamine domains and localization of phospholipid synthases in *Bacillus subtilis* membranes. *J Bacteriol*, **187**, 2163-2174.

Osumi, M., Konomi, M., Sugawara, T., Takagi, T. and Baba, M. (2006) High-pressure freezing is a powerful tool for visualization of Schizosaccharomyces pombe cells: ultra-low temperature and low-voltage scanning electron microscopy and immunoelectron microscopy. *J Electron Microsc (Tokyo)*, **55**, 75-88.

Sharpe, M.E., Hauser, P.M., Sharpe, R.G. and Errington, J. (1998) *Bacillus subtilis* cell cycle as studied by fluorescence microscopy: constancy of cell length at initiation of DNA replication and evidence for active nucleoid partitioning. *J Bacteriol*, **180**, 547-555.

Sipiczki, M. and Bozsik, A. (2000) The use of morphomutants to investigate septum formation and cell separation in Schizosaccharomyces pombe. *Arch Microbiol*, **174**, 386-392.

Stahlberg, H., Kutejova, E., Muchova, K., Gregorini, M., Lustig, A., Muller, S.A., Olivieri, V., Engel, A., Wilkinson, A.J. and Barak, I. (2004) Oligomeric structure of the *Bacillus subtilis* cell division protein DivIVA determined by transmission electron microscopy. *Mol Microbiol*, **52**, 1281-1290.

van den Ent, F. and Lowe, J. (2006) RF cloning: a restriction-free method for inserting target genes into plasmids. *J Biochem Biophys Methods*, **67**, 67-74.

Venema, G., Pritchard, R.H. and Venema-Schroeder, T. (1965) Fate of Transforming Deoxyribonucleic Acid in *Bacillus Subtilis*. *J Bacteriol*, **89**, 1250-1255.

Whitelam, S. and Geissler, P.L. (2007) Avoiding unphysical kinetic traps in Monte Carlo simulations of strongly attractive particles. *J Chem Phys*, **127**, 154101.

Zimmerman, S.B. and Minton, A.P. (1993) Macromolecular crowding: biochemical, biophysical, and physiological consequences. *Annu Rev Biophys Biomol Struct*, **22**, 27-65.

LEGENDS

Fig. S1: Formation of liposome clusters by DivIVA. Liposomes were stained with the fluorescent membrane dye Nile Red.

Fig. S2: (A) Size exclusion chromatography of DivIVA-MBP fusion proteins. 200 µg of each protein was loaded onto a Superose 6 gel filration column and eluted using a buffer containing 20 mM Tris-HCl pH 7.5 and 150 mM NaCl. The elution profiles were recorded by measuring UV absorption. The position of the molecular weight marker used for calibration is given at the top of the graph. The elution fractions were also analysed by SDS-PAGE (B).

Fig. S3: Time laps microscopy of *E. coli* cells expressing DivIVA-GFP. Time points are indicated in minutes.

Fig. S4: Bacterial two-hybrid interaction assay. *divIVA* and *racA* were cloned in different expression vectors and the combinations screened for adenylate cyclase activity (blue colony). A positive interaction was observed with a DivIVA-adenylate cyclase T25 fragment (low-copy plasmid p25-N) and an adenylate cyclase T18 fragment-RacA fusion (high-copy plasmid pUT18C). The different vectors are described in Table S1.

Fig. S5: Localization of DivIVA-GFP in *B. subtilis* mutants defective in the biosynthesis of phosphatidylglycerol (B; strain BSN7 grown without IPTG), phosphatidylethanolamine (C; strain BSN8), and cardiolipin (D; strain BSN9 grown without IPTG, E; strain BSN14 grown without IPTG). Wild type strain is shown in A.

Fig. S6: Binding of DivIVA to liposomes of different diameter (0.1, 0.4 and 5 μm). The DivIVA concentration was titrated (0.75, 0.38, and 0.19 μM), and the amount of DivIVA in the pellet fractions (arbitrary units) was determined by gel scanning. As a control the pellet fractions of reactions without liposomes are included.

Fig. S7: Measuring membrane curvature. Transmission electron microscopy picture of a *B. subtilis* division septum. Size measurements are indicated.

Fig. S8: Radius of membrane curvature at *S. pombe* cell division sites. The EM figures were copied from (Osumi et al., 2006; Sipiczki and Bozsik, 2000).

Fig. S9: Results of simulations run with different assumptions on the number of protein-protein and protein-membrane interactions. Columns A, B, and C show: the fraction of localized spheres as a function of the radius of curvature of the membrane, the density distributions at radii of curvature equal to 12.5 nm, and 50 nm, respectively. Case I; model with no restrictions on the total number of bonds. Parameters are: E_{pp} =2 kBT and E_{pm} =6 kBT. Case II; model with a restriction of maximum 4 bonds per sphere. A membrane contact counts as 1 protein-protein contact. Parameters are: E_{pp} =2.5 kBT and E_{pm} =5.5 kBT. Case III; model with a restriction of maximum 4 bonds per sphere. A membrane contact counts as 2 protein-protein contacts. Parameters are: E_{pp} =3 kBT and E_{pm} =5.5 kBT. Case IV; model with a restriction of maximum 6 bonds per sphere. A membrane contact counts as 3 protein-protein contacts. Parameters are: E_{pp} =3.5 kBT and E_{pm} =5.5 kBT. Case V; model with a restriction of maximum 8 bonds per sphere. A membrane contact counts as 4 protein-protein contacts. Parameters are: E_{pp} =3.5 kBT and E_{pm} =5.5 kBT. Case VI; model of rods. The

reaction conditions were essential as in case V, except that only 100 rods were used in the simulation.

Fig. S10: Modelling doggy bones as a stack of spheres. The figure (A) was copied from (Stahlberg et al., 2004). Lower panel (B) shows how 4 spheres fit the dimensions of a doggy bone.

Table S1: Bacterial strains and plasmids

B. subtilis	Relevant genotype[a, b]	construction or reference
3292	*divIVA-gfp:Cm amyE::(Pxyl-mreBCD Sp) mreB::Neo*	(Hamoen and Errington, 2003)
3310	*divIVA::Tet, minCD::Km*	(Edwards and Errington, 1997)
1803	*divIVA:(divIVA-gfp Cm)*	(Edwards et al., 2000)
LH60	*amyE::(divIVA amino acids 1-60 –GFP) divIVA::Tet minCD::Km*	this study
BFA2809	*pgsA::pMUTIN4*	(Kobayashi et al., 2003)
SDB01	*psd::Neo*	(Matsumoto et al., 1998)
SDB02	*pssA10::Sp*	(Matsumoto et al., 1998)
SDB206	*ywiE2::Neo ywjE::Sp clsA::pMutin4*	(Kawai et al., 2004)
BFS219	*clsA::pMutin4*	(Kawai et al., 2004)
BSN2	*amyE::(divIVA-gfp Sp)*	L. Hamoen, unpublished
BSN7	*amyE::(divIVA-gfp Sp) pgsA::pMUTIN4*	BSN2 transformed with BFA2809
BSN8	*amyE::(divIVA-gfp Sp) psd::Neo*	BSN2 transformed with SDB01
BSN9	*amyE::(divIVA-gfp Sp) clsA::pMutin4*	BSN2 transformed with BFS219
BSN13	*divIVA:(divIVA-gfp Cm) clsA::pMutin4*	1803 transformed with BFS219
BSN14	*divIVA:(divIVA-gfp Cm) ywiE2::Neo ywjE::Sp clsA::pMutin4*	1803 transformed with SDB206
E. coli		
MHD63	*Ami::Cm amiBC::Km Δslt*	(Korsak et al., 2005)
plasmid		
pSG1612	*divIVA-gfp*	(Edwards et al., 2000)
pQE60	*His6-tag expression vector*	Qiagen
pQEDG1	*divIVA-gfp-his6*	this study
pQEG2	*gfp-his10*	L. Hamoen, unpublished
pTYB1	*Intein-fusion expression vector*	New England Biolabs
pTBD1	*divIVA-intein*	this study
pMAL2-C2	*MBP-fusion expression vector*	New England Biolabs
pDM1	*divIVA-MBP*	this study
pDM2	*ΔC-DivIVA-MBP*	this study
pDM3	*ΔN-DivIVA-MBP*	this study
pRL10	*MBP-RacA fusion*	this study
pSG1154	*gfp-fusion vector for amyE integration*	(Lewis and Marston, 1999)
pDG7	*amy::divIVA-gfp Sp*	this study
pDG15	*DivIVA amino acids 1-60 -GFP*	this study
pDG13	*DivIVa aa 1-40 -GFP*	this study
pDG23	*V25E in first 60 amino acids of DivIVA-GFP*	this study
pDG26	*L29E in first 60 amino acids of DivIVA-GFP*	this study
pUT18-DivIVA	*T18 fragment of adenylate cyclase fused to the C-terminus of DivIVA, high copy plasmid*	R. Emmins, unpublished
p25-N-DivIVA	*T25 fragment of adenylate cyclase fused to the C-terminus of DivIVA, low copy plasmid*	R. Emmins, unpublished
pUT18C-DivIVA	*T18 fragment of adenylate cyclase fused to the N-terminus of DivIVA, high copy plasmid*	(Bramkamp et al., 2008)
pKT25-DivIVA	*T25 fragment of adenylate cyclase fused to the N-terminus of the DivIVA, low copy plasmid*	(Bramkamp et al., 2008)
pUT18-RacA	*T18 fragment of adenylate cyclase fused to the C-terminus of RacA, high copy plasmid*	this study
p25-N-RacA	*T25 fragment of adenylate cyclase fused to the C-terminus of RacA, low copy plasmid*	this study
pUT18C-RacA	*T18 fragment of adenylate cyclase fused to the N-terminus of RacA, high copy plasmid*	this study
pKT25-RacA	*T25 fragment of adenylate cyclase fused to the N-terminus of the RacA, low copy plasmid*	this study

[a]All *B. subtilis* strains carry the *trpC2* marker from the parental 168 strain.
[b]Antibiotics used for selection are indicated (Cm; chloramphenicol, Sp: spectinomycin, Km; kanamycin, Neo; neomycin, Tet; tetracycline).

Table S2: primers

primer	sequence	site
div1	CCCCGTCTCGCATGCCATTAACGCCAAATG	*BsmBI*
div2	CCCCGTCTCGGATCCTTCCTTTTCCTCAAATACAG	*BsmBI*
div20	GGTGGTTGCTCTTCCGCATTCCTTTTCCTCAAATA	*SapI*
div23	GGTGGTCATATGCCATTAACGCCAAATGA	*NdeI*
gfp7	AAGCTTGATATCGAATTCCTGCAGATGAGTAAAGG	
LH16	GCCGGCGAGAACAATTTCGTAATCTT	
LH20	GCCGGCAAAGTGTCCGATTCTTTCAT	
LH21	ATGCGCAAGAAAACTGAGCTTGA	
LH65	CGAGCACTTCACCAACAAGGACCATAGATTATGCCATTAACGCCAAATGA	
LH67	GATTACCAGTTTACCTTCTTCGATTTTCATGCTTCCTCCTTCCTTTTCCTCAAATACAG	
LH69	AATCTATGGTCCTTGTTGGT	
LH71	ATGAAAATCGAAGAAGGTAA	
LH77	TTTCAGAAGATCAAGCTGAG	
LH110	ATGAAGATGAAGAAAATGAATTCCT	
LH111	AGGAATTCATTTTCTTCATCTTCAT	
LH112	GTAAATGAATTCGAAGCCCAAGTCAG	
LH113	CTGACTTGGGCTTCGAATTCATTTAC	
RL 43	AACAATAACAACAACCTCGG GATCGAGGGAAGGATGAATACAAATATGGTAGCAAG	
RL 44	GTAAA ACGACGGCCAGTGCCAAGCTTGCCTTTAGGTTTGAAATTTGAACAGTG	

Fig. S1

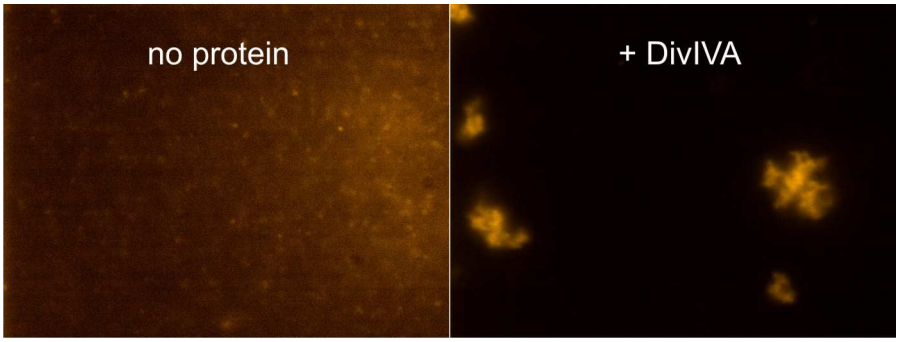

Fig. S2

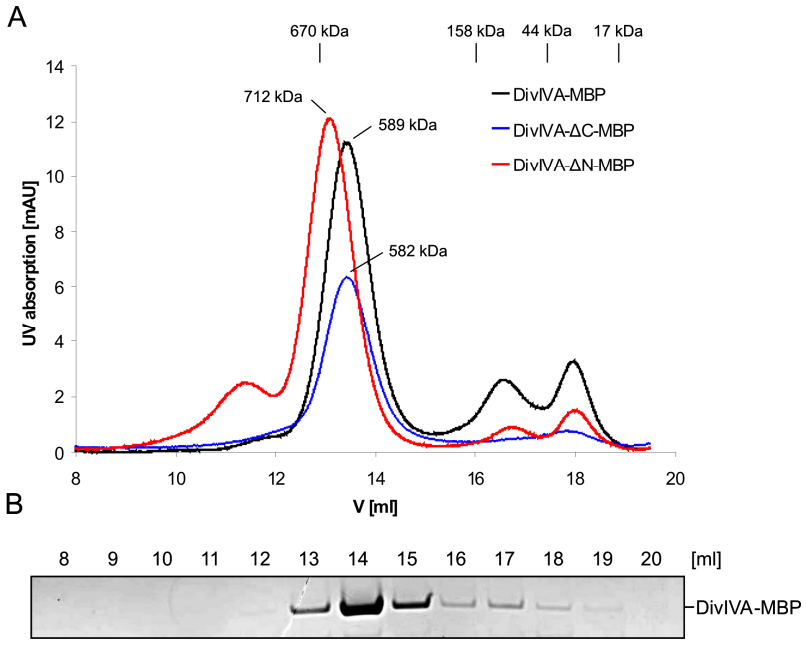
A
670 kDa
158 kDa
44 kDa
17 kDa
712 kDa
589 kDa
582 kDa
DivIVA-MBP
DivIVA-ΔC-MBP
DivIVA-ΔN-MBP
UV absorption [mAU]
V [ml]
B
8 9 10 11 12 13 14 15 16 17 18 19 20 [ml]
DivIVA-MBP

Fig. S3

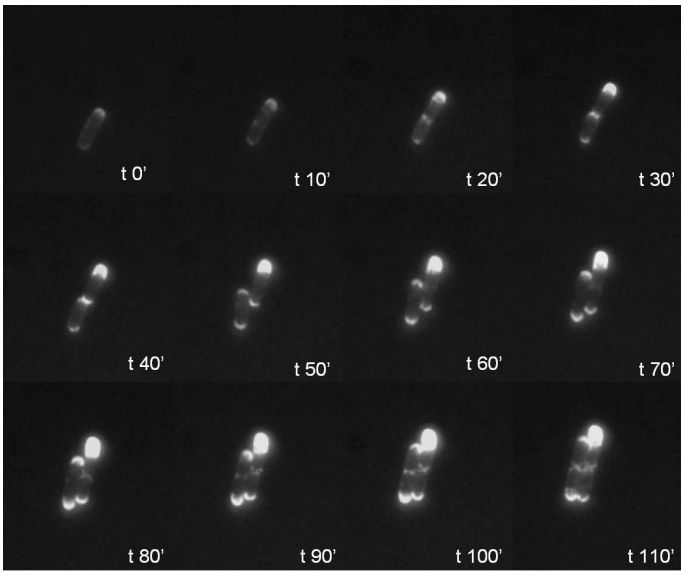

Fig. S4

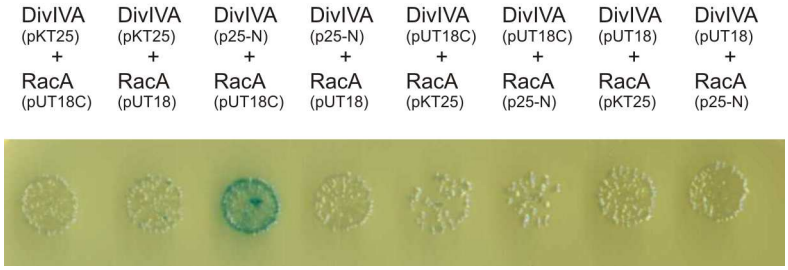
DivIVA (pKT25) + RacA (pUT18C)
DivIVA (pKT25) + RacA (pUT18)
DivIVA (p25-N) + RacA (pUT18C)
DivIVA (p25-N) + RacA (pUT18)
DivIVA (pUT18C) + RacA (pKT25)
DivIVA (pUT18C) + RacA (p25-N)
DivIVA (pUT18) + RacA (pKT25)
DivIVA (pUT18) + RacA (p25-N)

Fig. S5

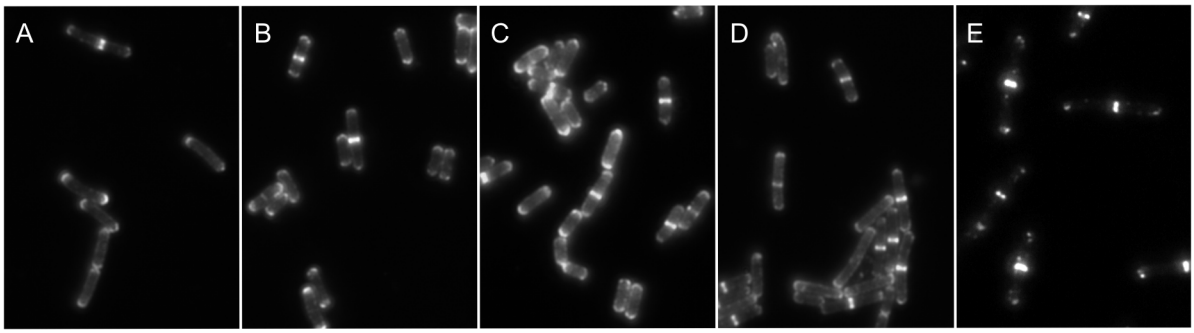

Fig. S6

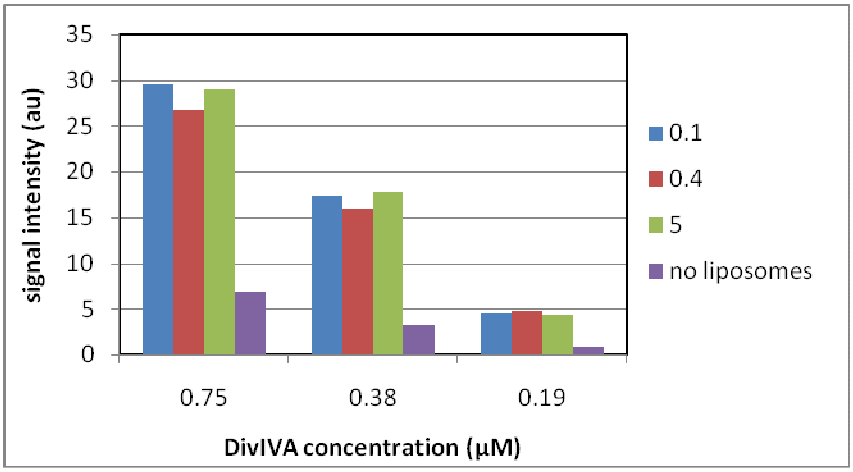
35
30
25
20
15
10
5
0
signal intensity (au)
0.75
0.38
0.19
DivIVA concentration (µM)
0.1
0.4
5
no liposomes

Fig. S7

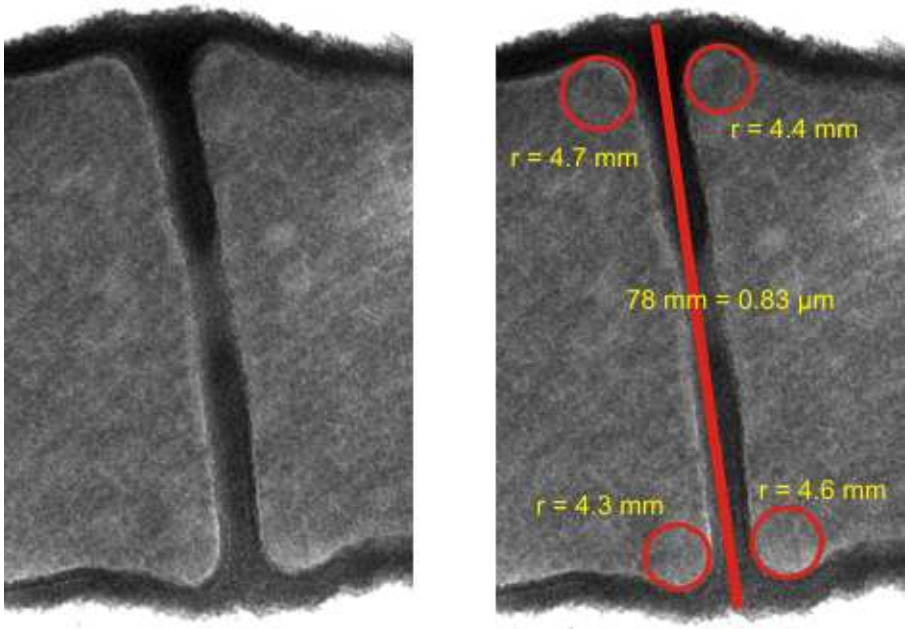

Fig. S8

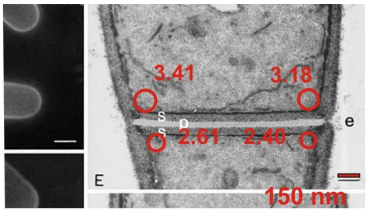

Sipiczki & Bozsik, 2000, Arch Mic

150 nm = 3.47

3.41
3.18
2.61
2.40
av. = 2.90 = 125 nm diameter
= 63 nm radius

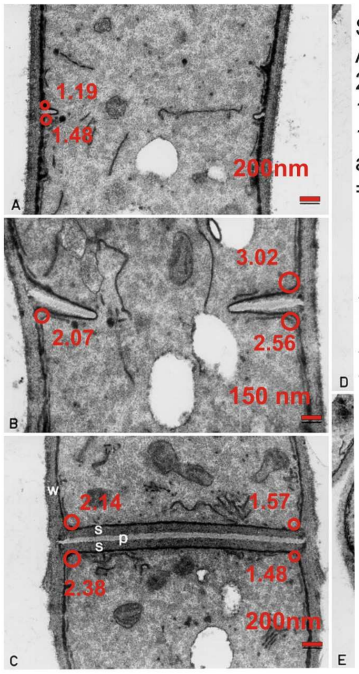

Sipiczki & Bozsik, 2000,
Arch Mic
200 nm = 3.22
1.19
1.48
av. = 1.34 = 83 nm diameter
= 42 radius

150 nm = 3.22
2.07
3.02
2.56
av. = 2.55 = 119 nm diameter
= 60 nm radius

200 nm = 3.22
2.14
2.38
1.57
1.48
av. = 1.89 = 118 nm diameter
= 59 nm radius

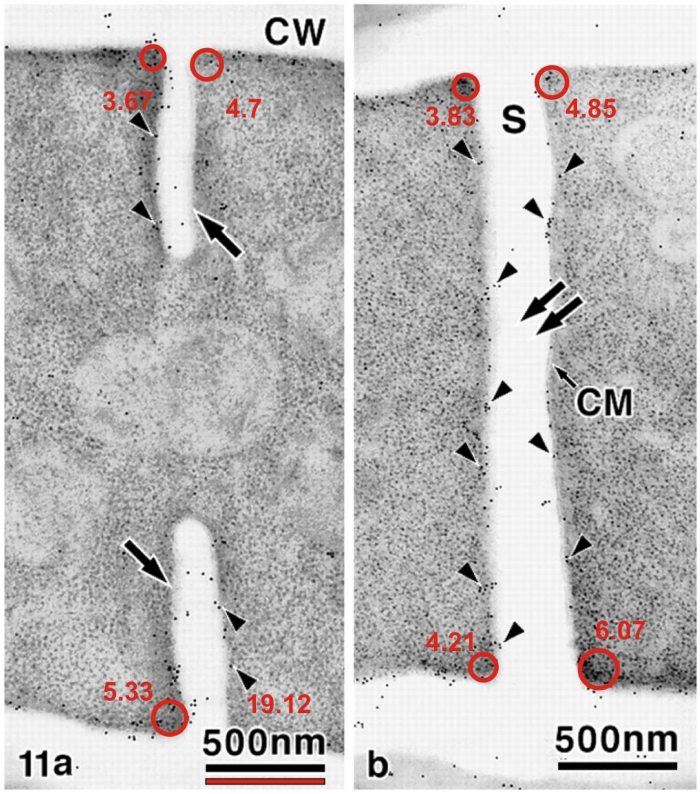

Osumi et al., 2006, J.
Eletronc Mic.

500 nm = 19.12

3.67
4.7
3.83
4.85
5.33
4.21
6.07

av. = 4.67 = 122 nm diameter
= 61 nm radius

Fig. S9

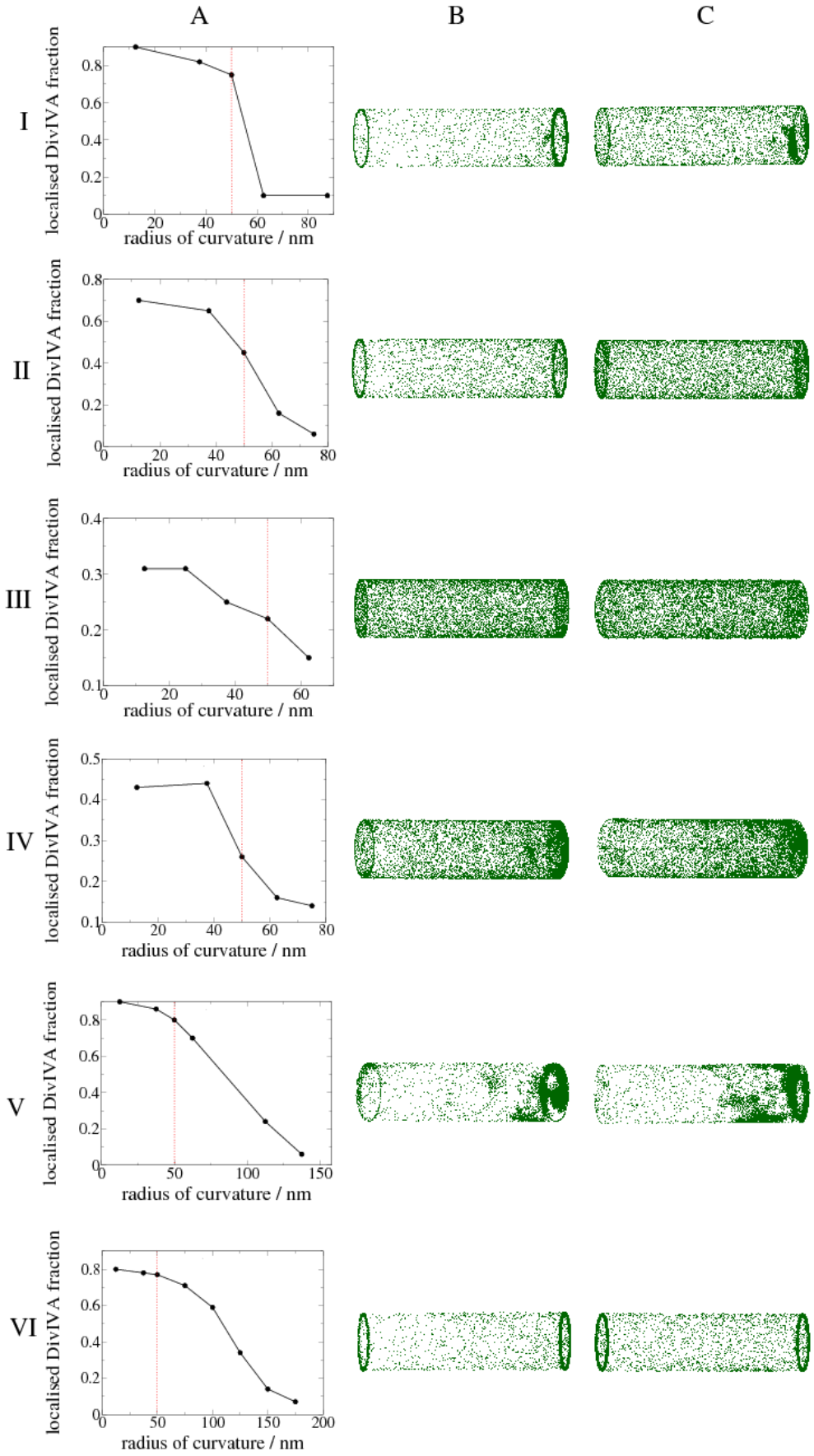
A
B
C
I
II
III
IV
V
VI
localised DivIVA fraction
radius of curvature / nm

Fig. S10